Epsilon-near-zero response and tunable perfect absorption in Weyl semimetals

Klaus Halterman,[1] Mohammad Alidoust,[2] and Alexander Zyuzin[3,4]

[1]*Michelson Laboratory, Physics Division, Naval Air Warfare Center, China Lake, California 93555, USA*
[2]*Department of Physics, K.N. Toosi University of Technology, Tehran 15875-4416, Iran*
[3]*Department of Applied Physics, Aalto University, P. O. Box 15100, FI-00076 AALTO, Finland*
[4]*Ioffe Physical-Technical Institute, St. Petersburg 194021, Russia*

We theoretically study the electromagnetic response of type-I and type-II centrosymmetric Weyl metals. We derive an anisotropic permittivity tensor with off-diagonal elements to describe such gyrotropic media. Our findings reveal that for appropriate Weyl cones tilts, the real part of the transverse component of the permittivity can exhibit an ϵ-near-zero response. The tilt parameter can also control the amount of loss in the medium, ranging from lossless to dissipative when transitioning from type-I to type-II. Similarly, by tuning either the frequency of the electromagnetic field or the chemical potential in the system, an ϵ-near-zero response can appear as the permittivity of the Weyl semimetal transitions between positive and negative values. Employing the obtained permittivity tensor, we consider a setup where the Weyl semimetal is deposited on a perfect conductive substrate and study the reflection and absorption characteristics of this nano-layered configuration. We show that by choosing the proper geometrical and material parameters, devices can be created that perfectly absorb electromagnetic energy over a wide angular range of incident electromagnetic waves.

I. INTRODUCTION

Since the advent of metamaterials, efforts to design materials that can be used to control electromagnetic (EM) fields has flourished. One prominent route involves developing anisotropic structures whose EM response is described by a permittivity tensor $\bar{\bar{\epsilon}}$ that has components with extreme values, including ϵ-near-zero (ENZ) [1] media, where the real part of a component of $\bar{\bar{\epsilon}}$ vanishes along a given coordinate axis. Within the ENZ regime, the phase of the entering EM wave can be uniform, and the wavefront conforms to the shape of the exit side of the ENZ medium [2]. A number of ENZ-based architectures have been fabricated, including subwavelength dielectric coatings that control the resonant coupling of light with ENZ regions [3]. Experimental work with microwave waveguides [4,5] demonstrated how a narrow ENZ channel can lead to enhanced electromagnetic coupling. A nanoparticle mixture containing dielectric and metal constituents with an effective ENZ response exhibited an increase in the superconducting critical temperature [6]. The propagation of a transverse magnetic optical beam through a subwavelength slit demonstrated a transmission enhancement [7] when the InAsSb semiconductor substrate was tuned to its ENZ frequency.

Many pathways have been studied that lead to the creation of ENZ materials, including intricate combinations of metal-dielectric multilayers and arrays of rods, or transparent conducting oxides. Other approaches involve the use of more exotic materials like graphene [8] with its intrinsic two dimensionality and linear dispersion around the Dirac point. Recently, Weyl semimetals [9–16] have been added to the ever-expanding class of materials that have unconventional EM properties. The band structure of a Weyl semimetal (WS) is characterized by a conical energy spectrum with an even number of Weyl nodes that are topologically protected. The chiralities of Weyl nodes correspond to topological charges that result in monopoles and antimonopoles in the Berry curvature [11,12]. Indeed, the Weyl semimetal phase manifests itself in unusual surface states with Fermi arcs [17] and chiral anomalies [10–13,16]. Weyl semimetals are topologically nontrivial materials that are predicted for the magnetic compounds Y_2IrO_7, Eu_2IrO_7, and $HgCr_2Se_4$ [18,19], and in some nonmagnetic samples, including TaAs, TaP, NbAs [20], and NbP [11,21–24]. The WS TaAs was shown to have a wide spectral range as a room-temperature photodetector [25].

The synthesis of different alloys into Weyl semimetal crystals can result in an unusual type of Weyl semimetal that is characterized by titled Weyl nodes and an open Fermi surface. This class of Weyl semimetals is identified as type-II if the tilt of the Weyl cone exceeds the Fermi velocity [9,26–32]. Since condensed matter systems do not require Lorentz invariance, Weyl semimetals are not restricted to closed point-like Fermi surfaces and support type-II Weyl fermions [9,26,33,34]. This type of Weyl fermion appears at the boundary between electron and hole pockets [9,26]. The experimental signatures of this phase were recently reported in Refs. [28,29]. The effects of Weyl cone tilt on the optical conductivity and polarization was recently studied [35]. The effect of a tilt on the absorption of circular polarized light was studied for both type-I and type-II cases and it was shown that by reversing the tilting direction of Weyl nodes the right-hand and left-hand responses of Weyl semimetal become reversed [36]. Also, it was found that chirality or the tilt sign in Weyl semimetals with tilted cones in the absence of time-reversal and inversion symmetries can change the sign of the Weyl contribution to the absorptive Hall conductivity [37].

Tunable metamaterial absorbers with active materials have been explored with a variety of different materials [38–41]. The broad tunability of the chemical potential in a WS makes it a promising material for photonics and plasmonics applications [42–52]. The chiral anomaly in a WS can alter surface plasmons and the EM response [42,47–52]. It has been shown theoretically [51] that measurements of the optical conductivity and the temperature dependence of the free carrier response in pyrochlore $Eu_2Ir_2O_7$ are consistent with the WS phase. Also, the interband optical conductivity reduces to zero in a continuous fashion at low frequencies, as predicted for a WS. The analysis of experimental data resulted in a Fermi velocity on the order of $v_F \approx 4 \times 10^7$ cm/s [47,51]. The surface magnetoplasmons of a Weyl semimetal can turn to low-loss localized guided modes when two crystals of the WSs with different magnetization orientations are connected [42].

In this paper, we study the anisotropic electromagnetic response of both type-I and type-II Weyl semimetals. Our study includes both analytic and numerical results that reveal the behavior of each component of the dielectric tensor as a function of the Weyl cone tilt, chemical potential, and EM wave frequency. We show that by appropriately tailoring these system parameters, the real part of the transverse component of the permittivity can achieve an ENZ response. In parallel, we also demonstrate how the dissipative effects in the medium can be controlled. Utilizing the derived permittivity tensor and its subsequent numerical analysis, we consider a Weyl semimetal (both types I and II) on top of a perfectly conducting substrate and study the absorption properties of an incident electromagnetic wave from vacuum into the Weyl semimetal. Solving Maxwell's equations, we derive the reflection and absorption coefficients and show that by properly choosing material and geometric parameters, tunable coherent perfect absorption is feasible over a wide range of incident angles.

The paper is organized as follows. In Sec. II, we present the derived permittivity tensor applicable to both type-I and type-II WSs. We apply various approximations and discuss the EM response of type-I and type-II WSs in Subsecs. II B and II C, respectively. In Subsec. II D, we numerically illustrate and analyze various features of both types of WSs. In Sec. III, we present a practical application of the analyses given in Sec. II. In particular, we study the electromagnetic response of a WS grounded by a perfect conductor. Starting from Maxwell's equations, we derive analytical expressions for the reflection and absorption coefficients of this structure as a function of incident electromagnetic wave angle and thickness of the WS. Furthermore, we numerically analyze various aspects of the absorption characteristics of this system. Finally, we give concluding remarks in Sec. IV.

II. APPROACH AND RESULTS

In this section, we outline the model Hamiltonian and calculate the permittivity tensor for both a type-I and type-II WS. General expressions are given for determining each of the permittivity components, and analytic results are derived for various limiting cases. Results are then presented for the susceptibility and ϵ-near-zero response as a function of frequency ω, chemical potential μ, and tilt parameter β.

A. Permittivity tensor

Throughout this paper, we focus on a model Hamiltonian with broken time-reversal symmetry and only two Weyl nodes. This model can be achieved through the stacking of multiple thin films involving a topological insulator and ferromagnet blocks, as first proposed theoretically [10]. The Hamiltonian describing the low-energy physics around the two Weyl nodes, defined by $s = \pm$, is given by

$$H_s(\mathbf{p}) = v_F[\beta_s(p_z - sQ) + s\boldsymbol{\sigma}(\mathbf{p} - sQ\mathbf{e}_z)]. \quad (1)$$

Here $\mathbf{e}_z$ is the unit vector along the z direction, and we take the Fermi velocity v_F to be positive. The separation between two Weyl points in the z direction in momentum space is defined by $2|Q|$, where the sign of Q depends on the orientation of magnetization with respect to the quantization axis. The quantities $\beta_\pm$ are tilting parameters that control the transition between the type-I and type-II phases. For centrosymmetric materials with broken time-reversal symmetry, we apply the condition $\beta_+ = -\beta_-$. The corresponding electron Green's functions are given by

$$G_s(\varepsilon_n, \mathbf{p}) = \frac{1}{2} \sum_{t=\pm 1} \frac{1 + st\boldsymbol{\sigma}\mathbf{p}^{(s)}/|\mathbf{p}^{(s)}|}{i\varepsilon_n + \mu - v_F[\beta_s p_z^{(s)} + t|\mathbf{p}^{(s)}|]}, \quad (2)$$

where the index t identifies each of the two subbands, $\mathbf{p}^{(s)} = \mathbf{p} - sQ\mathbf{e}_z$, and μ is the chemical potential, in which we set $\mu \geqslant 0$ without loss of generality. The fermionic Matsubara frequency is $\varepsilon_n = \pi T(2n + 1)$, in which T represents temperature and n is an integer. The dielectric function $\epsilon_{ab}(\omega)$ (where $a, b \equiv x, y, z$) is defined through the optical conductivity σ_{ab} via

$$\sigma_{ab}(\omega) = \frac{i}{\omega} \lim_{|\mathbf{q}| \to 0} [\Pi_{ab}(\omega, \mathbf{q}) - \Pi_{ab}(0, \mathbf{q})], \quad (3)$$

$$\epsilon_{ab}(\omega) = \delta_{ab} + i \frac{\sigma_{ab}(\omega)}{\epsilon_0 \omega},$$

where ϵ_0 is the permittivity of free space and the current-current correlation function reads

$$\Pi_{ab}(\omega, \mathbf{q}) = e^2 T \sum_n \sum_{s=\pm} \text{Tr} \int \frac{d^3 p}{(2\pi)^3} J_{a,s} G_s(\varepsilon_n + \omega_k, \mathbf{p} + \mathbf{q})$$
$$\times J_{b,s} G_s(\varepsilon_n, \mathbf{p})\}|_{i\omega_k \to \omega + i\delta}, \quad (4)$$

where $\mathbf{J}_s = v_F(\beta_s\mathbf{e}_z + s\boldsymbol{\sigma})$, $\omega_k = 2\pi Tk$ is the bosonic Matsubara frequency and k is an integer. Thus, the permittivity tensor $\bar{\bar{\epsilon}}$ takes the following gyrotropic form that is valid for both type-I and type-II Weyl semimetal phases:

$$\bar{\bar{\epsilon}} = \begin{pmatrix} \epsilon_{xx}(\omega) & \epsilon_{xy}(\omega) & 0 \\ \epsilon_{yx}(\omega) & \epsilon_{yy}(\omega) & 0 \\ 0 & 0 & \epsilon_{zz}(\omega) \end{pmatrix}, \quad (5a)$$

where the off-diagonal components are given by $\epsilon_{xy}(\omega) = -\epsilon_{yx}(\omega) = i\gamma(\omega)$. These terms can lead to modified polarization rotations via the Kerr and Faraday effects [53,54]. Variations in the gyrotropic term can also cause shifts in the surface plasmon frequency [55]. The $\epsilon_{xx,yy}(\omega)$ components are equal and can be written analytically as

$$\epsilon_{xx,yy}(\omega) = 1 + \frac{\alpha}{3\pi}\left[\ln\left|\frac{4\Gamma^2}{4\mu^2 - \omega^2}\right| - \frac{4\mu^2}{\omega^2} + i\pi\Theta(\omega - 2\mu)\right], \quad (5b)$$

in which $\alpha = e^2/(4\pi\epsilon_0\hbar v_F)$ and $\Gamma \sim v_F|Q|$, such that $\Gamma \gg (\omega, \mu)$ is the high-energy cutoff where applicability of the linear model no longer holds. Here $\Theta(X)$ represents the

usual step function. The remaining components involve integrals, which for $\Gamma \gg (\omega, \mu)$, are written in the limit of zero temperature:

$$\epsilon_{zz}(\omega) = 1 - \frac{\pi\alpha}{\omega^2}\sum_{t=\pm 1}\sum_{s=\pm}\int\frac{d^3p}{(2\pi)^3}\left[-\frac{p_\perp^2 t\omega_k^2/4}{p^3(p^2+\omega_k^2/4)}\Theta(\mu - \zeta_{s,t}) + \left(\beta_s + t\frac{p_z}{p}\right)^2\delta(\mu - \zeta_{s,t})\right]\Bigg|_{i\omega_k\to\omega+i\delta}. \tag{5c}$$

It is convenient to separate Fermi surface and vacuum contributions to $\gamma(\omega) = \sum_{s=\pm}[\gamma_{FS}^{(s)}(\omega) + \gamma_0^{(s)}(\omega)]$, where

$$\gamma_{FS}^{(s)}(\omega) = \frac{s\alpha}{\omega^2}\int_0^\infty\frac{p_\perp dp_\perp}{2\pi}\int_{-\Gamma-sv_FQ}^{\Gamma-sv_FQ}dp_z\frac{p_z}{p}\frac{i\omega_k}{p^2+\omega_k^2/4}[\Theta(\mu-\zeta_{s,+})-\Theta(\mu-\zeta_{s,-})-1]|_{i\omega_k\to\omega+i\delta}, \tag{5d}$$

$$\gamma_0^{(s)}(\omega) = \frac{s\alpha}{\omega^2}\int_0^\infty\frac{p_\perp dp_\perp}{2\pi}\int_{-\Gamma_0-sv_FQ}^{\Gamma_0-sv_FQ}dp_z\frac{p_z}{p}\frac{i\omega_k}{p^2+\omega_k^2/4}\Bigg|_{i\omega_k\to\omega+i\delta}, \tag{5e}$$

in which we have defined $\zeta_{s,t} \equiv tp + p_z\beta_s$, $p = \sqrt{p_z^2 + p_\perp^2}$, and a momentum cutoff along the z axis, Γ. Generally, the cutoff Γ is a function of the tilt parameter. Nevertheless, in our calculations, we choose a large enough cutoff and neglect the contribution of β to Γ. The cutoff $\Gamma_0 > v_F|Q|$ is introduced for the correct definition of the vacuum contribution.

B. Zero-tilt phase: $\beta = 0$

It is evident that $\epsilon_{xx,yy}(\omega)$ are independent of the tilting parameters β_s. To reduce $\bar{\bar{\epsilon}}$ to the situation where the Weyl nodes experience no tilt, it suffices to set $|\beta_+| = |\beta_-| = 0$. In this case, $\epsilon_{zz}(\omega) = \epsilon_{xx,yy}(\omega)$, and the off-diagonal frequency dependent component $\gamma(\omega)$ reduces to

$$\gamma(\omega) = \frac{2\alpha}{\pi}\frac{v_F Q}{\omega}. \tag{6}$$

The gyrotropic parameter $\gamma(\omega)$ can play an important role in changing the polarization state of electromagnetic waves interacting with the WS via Faraday and Kerr rotations [54]. The imaginary term in Eq. (5b) describes the interband contribution to the optical conductivity, which exists only when the frequency ω of the EM wave satisfies $\omega > 2\mu$. The interval of frequencies in which $\epsilon_{xx,yy}$ is real and positive correspond to

$$2\mu > \omega > 2\mu\sqrt{\frac{\alpha}{3\pi\left(1 + \frac{2\alpha}{3\pi}\ln\left|\frac{\Gamma}{\mu}\right|\right)}}. \tag{7}$$

Thus, for frequencies around the chemical potential, $2\mu > \omega \gtrsim \mu$, the diagonal components $\epsilon_{xx,yy}$ do not contribute to dissipation in the medium. On the other hand, if $\omega > 2\mu$, $\epsilon_{xx,yy}$ acquires an imaginary part, leading to dissipation.

C. Finite tilt phase: $\beta \neq 0$

We now examine some limiting cases for the integrals in Eqs. (5c) and (5d) when the tilting parameter is nonzero. At

the charge neutrality point, $\mu = 0$, the off-diagonal gyrotropic component $\gamma(\omega)$ reduces to

$$\gamma(\omega) = \frac{\alpha}{\pi}\frac{v_F Q}{\omega}[\min(1, |\beta_+|^{-1}) + \min(1, |\beta_-|^{-1})]. \tag{8}$$

It is seen that $\gamma(\omega)$ is independent of the tilt parameter if $|\beta_s| < 1$, while inversely proportional to it when $|\beta_s| > 1$. The ϵ_{zz} component of the dielectric tensor in the limit of zero chemical potential, $\mu = 0$, can be calculated exactly as well. For $|\beta_s| < 1$, we find

$$\epsilon_{zz} = 1 + \frac{\alpha}{3\pi}\left[\ln\left|\frac{4\Gamma^2}{\omega^2}\right| + i\pi\Theta(\omega)\right], \tag{9}$$

and when the tilt parameter satisfies $|\beta_s| > 1$, we arrive at

$$\epsilon_{zz} = 1 + \frac{\alpha}{3\pi}\left[\ln\left|\frac{4\Gamma^2}{\omega^2}\right| + i\pi\Theta(\omega)\right]\sum_{s=\pm}\frac{1}{4|\beta_s|}\left(3 - \frac{1}{\beta_s^2}\right)$$
$$- \frac{\alpha\Gamma^2}{\pi\omega^2}\sum_{s=\pm}|\beta_s|\left(1 - \frac{1}{\beta_s^2}\right)^2. \tag{10}$$

Here, the last term describes the contribution from the Fermi pocket, which is bounded by Γ/v along the z axis in momentum space, thus demonstrating that the real part of ϵ_{zz} is always positive and independent of the tilt parameters if $|\beta_s| < 1$. Only when the conical tilt parameters exceed unity ($|\beta_s| > 1$) can the real part of ϵ_{zz} become negative or zero, thus allowing for the possibility of an ENZ response. Note that the amplitude of the imaginary component declines monotonically with increasing the tilt parameter β.

We now turn our attention to the tilted case when the chemical potential is finite. In general, the integral in Eq. (5c) for ϵ_{zz} is highly complicated, and solutions must be obtained numerically. Nonetheless, when $|\beta_s| < 1$, it is possible to

approximate ϵ_{zz} as follows:

$$\epsilon'_{zz} = 1 + \frac{\alpha\mu^2}{\pi\omega^2} \sum_{s=\pm} \frac{1}{\beta_s^3} \left\{ \frac{8}{3}\beta_s - 4\arctanh\beta_s + \ln\left|\frac{4\mu^2 - \omega^2(1+\beta_s)^2}{4\mu^2 - \omega^2(1-\beta_s)^2}\right| \right.$$

$$\left. + \frac{\omega^2}{12\mu^2} \sum_{t=\pm 1} \left[t(1+2t\beta_s)(1-t\beta_s)^2 \ln\left|\frac{4\Gamma^2(1-t\beta_s)^2}{4\mu^2 - \omega^2(1-t\beta_s)^2}\right| - \frac{2\mu}{\omega}\left(\frac{4\mu^2}{\omega^2} + 3 - 3\beta_s^2\right) \ln\left|\frac{2\mu - t\omega(1+t\beta_s)}{2\mu + t\omega(1+t\beta_s)}\right| \right] \right\},$$

$$(11a)$$

$$\epsilon''_{zz} = \frac{\alpha}{6}\sum_{s=\pm}\Theta\left(\omega - \frac{2\mu}{1+|\beta_s|}\right)\left\{1 - \frac{1}{2}\left[1 + \frac{3}{2|\beta_s|}\left(\frac{2\mu}{\omega} - 1\right)\left(1 - \frac{1}{3\beta_s^2}\left\{\frac{2\mu}{\omega} - 1\right\}^2\right)\right]\Theta\left(\frac{2\mu}{1-|\beta_s|} - \omega\right)\right\}, \quad (11b)$$

where we have decomposed the permittivity into its real and imaginary components: $\epsilon_{zz} = \epsilon'_{zz} + i\epsilon''_{zz}$. If $|\beta_-| = |\beta_+| \equiv |\beta|$, the imaginary part of ϵ_{zz} is zero when $\omega < 2\mu/(1+|\beta|)$ and increases as a function of ω in the interval $2\mu/(1+|\beta|) < \omega < 2\mu/(1-|\beta|)$. This expression is independent of frequency if $\omega > 2\mu/(1-|\beta|)$. Next, if we consider the limit $|4\mu^2 - \omega^2|^{1/2} \gg \mu|\beta_s|$, we find that ϵ_{zz} takes the following form:

$$\epsilon_{zz} = 1 + \frac{\alpha}{3\pi}\left[\ln\left|\frac{4\Gamma^2}{4\mu^2 - \omega^2}\right| - \frac{4\mu^2}{\omega^2} + i\pi\Theta(\omega - 2\mu)\right.$$

$$\left. - \frac{8\mu^4}{\omega^2}\frac{12\mu^2 - 5\omega^2}{5(4\mu^2 - \omega^2)^2}(\beta_-^2 + \beta_+^2)\right], \quad (12)$$

where the last term can be viewed as a correction arising from the tilt of the Weyl cones. Finally, in the limit $\omega \to 0$, the off-diagonal component has the form

$$\gamma = \frac{\alpha}{\pi\omega}\left[2v_F Q - \sum_{s=\pm}\frac{s\mu}{2\beta_s}\left(\frac{1}{\beta_s}\ln\left|\frac{1+\beta_s}{1-\beta_s}\right| - 2\right)\right],$$

$$|\beta_s| \ll 1, \quad (13a)$$

$$\gamma = \frac{\alpha}{\pi\omega}\sum_{s=\pm}\left[\frac{v_F Q}{|\beta_s|} - \frac{s\mu}{2\beta_s}\ln\left|\beta_s^2\frac{\Gamma}{\mu}\right|\right], \quad |\beta_s| \gg 1. \quad (13b)$$

Thus, for fixed β, these expressions show that for small values of the tilt parameter, γ is linear function of μ, declining as the chemical potential increases. For $\beta \gg 1$, γ strongly diminishes with μ, eventually changing sign. If on the other hand, we have a set chemical potential, increasing the tilt also reduces the gyrotropic effect by weakening γ, and more rapidly for larger μ. In both regimes, at a vanishing chemical potential $\mu \to 0$, we recover our previously discussed results at the charge neutrality point.

D. Susceptibility and ϵ-near-zero responses

When characterizing the nontrivial behavior of $\overline{\overline{\epsilon}}$ in the WS, there are several relevant parameters to consider, including the chemical potential, frequency of the EM wave, tilt of the Weyl cones, and the node separation parameter Q, which is taken to be positive. Although it may be possible to generate a mixture

of type-I and type-II Weyl points [56], we consider here the simpler configuration where $\beta_+ = -\beta_- = \beta$. In presenting the results, we write ω in units of energy, and the complex component ϵ_{zz} is written in terms of its real and imaginary parts: $\epsilon_{zz} = \epsilon'_{zz} + i\epsilon''_{zz}$. When presenting results, we plot the normalized susceptibility χ_{zz}, defined as $\chi_{zz} \equiv (\epsilon'_{zz} - 1)3\pi/\alpha$. Therefore, the ENZ regime corresponds to $\chi_{zz} = -3\pi/\alpha$. We also normalize the dissipative component by α. One of the primary aims is to locate in parameter space, the particular ω, μ, and β that result in the real part of $\epsilon_{zz} \sim 0$. Therefore, when varying the chemical potential in the WS, we consider a dimensionless μ ranging from the charge neutrality point, $\mu = 0$, up to $\mu/(v_F|Q|) = 0.5$. Similarly, in order to have as complete a picture as possible, a wide spectrum of dimensionless frequencies is considered corresponding to $0.05 \leqslant \omega/(v_F|Q|) \leqslant 1$. When the frequency is not varying, we set it to its dimensionless value of $\omega/(v_F|Q|) = 0.3$. Of particular importance is the tilt of the Weyl cones, which determines the corresponding μ and ω that lead to a vanishing of the real part of ϵ_{zz}. A broad range of cone inclinations covering both type-I and type-II scenarios is therefore examined. When computing the integrals, it is necessary to specify an energy cutoff Γ. Here we set $\Gamma/(v_F|Q|) \sim 8$, recalling that the linearized model breaks down when $\Gamma > v_F|Q|$, and which is consistent with the requirement $\Gamma \gg (\omega, \mu)$ discussed in conjunction with Eq. (5b). Since the linear model is most suitable away from the Lifshitz transition between type-I and type-II Weyl semimetals, a qualitatively correct description of the system can still be obtained with the linearized model near the transition by simply taking either larger cutoffs or by incorporating higher order momenta into the linear model.

To begin, in Fig. 1, we examine the frequency response of the normalized susceptibility χ_{zz} and ϵ''_{zz} over a broad range of β. The other diagonal components can be compared by examining the $\beta = 0$ cases, whereby $\epsilon_{xx,yy} = \epsilon_{zz}$. When $\mu = 0$, we calculate ϵ_{zz} using Eq. (9) for $\beta < 1$ and Eq. (10) for $\beta > 1$. For finite μ and $\beta < 1$, we utilize the expressions in Eqs. (11a) and (11b). If, however, the WS is type-II with $\beta > 1$, we must resort to the general integral in Eq. (5c) and solve for ϵ_{zz} numerically. The results are separated into three columns, where each column represents a different chemical potential, as labeled. Figures 1(a) and 1(b) show χ_{zz} and ϵ_{zz} for $\mu/(v_F|Q|) = 0$, Figs. 1(c) and 1(d) correspond to $\mu/(v_F|Q|) = 0.2$, and Figs. 1(e) and 1(f) have $\mu/(v_F|Q|) = 0.4$. Beginning with the charge neutrality point,
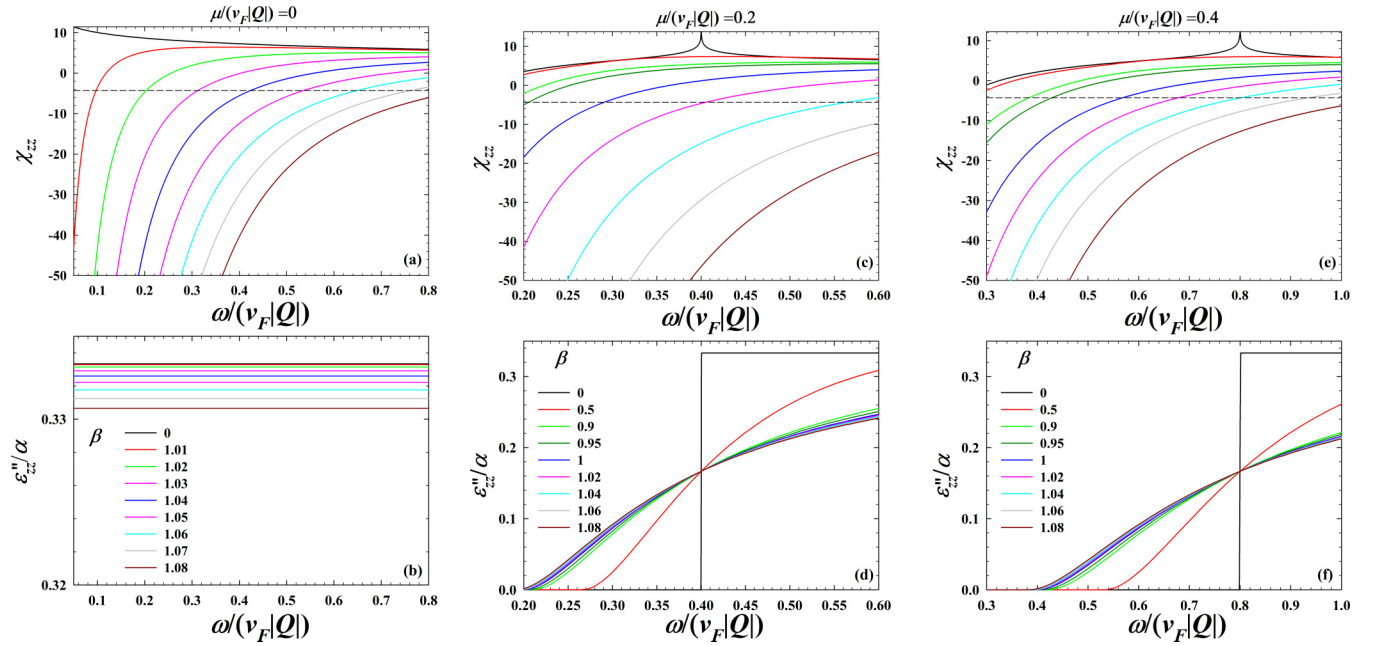
FIG. 1. Representative behavior of the permittivity ϵ_{zz} as a function of frequency. The top row corresponds to the normalized susceptibility χ_{zz}, while the bottom row is the imaginary component ϵ''_{zz}/α. The dashed lines identify points where an ENZ response arises. The tilting of the Weyl cones are seen to have a significant effect in creating an ENZ response. The corresponding β are depicted in the legends. The effects of altering the chemical potential is also shown, where each column depicts one of the three different μ considered. [(a), (b)] $\mu/(v_F|Q|) = 0$, [(c), (d)] $\mu/(v_F|Q|) = 0.2$, and [(e), (f)] $\mu/(v_F|Q|) = 0.4$.

$\mu/(v_F|Q|) = 0$, we see in Figs. 1(a) and 1(b) that for $\beta \leqslant 1$, χ_{zz} remains positive over the given frequency range, similar to a conventional dielectric. As β increases, and the system transitions toward a type-II WS ($\beta > 1$), the susceptibility gets shifted down overall, leading to regions where $\epsilon'_{zz} < 0$. Indeed, within the type-II regime and $\beta \gg 1$, the ENZ frequency can be found from Eq. (10) to be approximately written as

$$\omega_{\mathrm{ENZ}}^2 \approx \frac{2\alpha}{\pi}|\beta|\Gamma^2. \tag{14}$$

The dissipative component does not depend on frequency, and for $\beta \gg 1$, declines toward zero.

Next, in Figs. 1(c) and 1(d), the normalized chemical potential is increased to $\mu/(v_F|Q|) = 0.2$, so that now the frequency range of interest is shifted accordingly. The top panel shows that for the case $\beta = 0$, a peak in χ_{zz} arises. This peak emerges due to the interband transition, which leads to the singularity arising from the logarithmic term at $\omega = 2\mu$ in Eq. (5b). For most β, we again find at the lowest frequencies, $\epsilon'_{zz} < 0$, similar to the behavior of some metals at optical frequencies. Upon increasing ω, ϵ'_{zz} increases until arriving at the ENZ frequency where $\epsilon'_{zz} = 0$. Figure 1(d) exhibits the dissipation characteristics of this WS. There are now several distinct features that ϵ''_{zz} has compared to the $\mu = 0$ case. In particular, for $\beta = 0$, the imaginary component abruptly changes from lossless to lossy at the frequency $\omega = 2\mu$. Increasing β causes the dissipation at the transition point to broaden, until $\beta = 1$, after which the imaginary component becomes independent of the tilt parameter. Note that for $\beta < 1$, ϵ''_{zz} vanishes for $\omega \lesssim 2\mu/(1+\beta)$, and increases as a function of ω in the interval $2\mu/(1+\beta) < \omega < 2\mu/(1-\beta)$ [see Eq. (11b)]. Lastly, in Figs. 1(e) and 1(f), a larger

chemical potential corresponding to the dimensionless value of $\mu/(v_F|Q|) = 0.4$ is considered. It is observed that when increasing μ, there is a widening of the frequency window in which the ENZ response occurs. There is also a broadening of the imaginary component, resulting in finite dissipation over more frequencies.

One of the salient features of Weyl semimetals is the ability to systematically change their chemical potential. It is possible to shift μ about the charge neutrality point through doping, varying the temperature, or altering the lattice constant of the material through pressure variations [24,43,44]. For instance, upon raising the temperature, the number of thermally excited charged carriers increases near the Weyl points, increasing the chemical potential [43]. The injection of various dopants into the Weyl semimetal also can increase the number of free charged carriers, depending on the dopant type [44,45,47]. To examine how changes in μ can alter the EM response of a WS, we examine in Fig. 2(a) χ_{zz} and in Fig. 2(b) the dimensionless ϵ''_{zz} as functions of μ. Figure 2(a) shows that for $\beta \leqslant 1$ and $\mu = 0$, all curves originate at $\chi_{zz} = \ln(4\Gamma^2/\omega^2) \approx 7.85$ [see Eq. (9)]. For Weyl cones that are tilted with $\beta \leqslant 1$, increasing μ causes a splitting of the curves which then monotonically decline. Further increases in β causes χ_{zz} to shift downward, becoming negative for all μ. Figure 2(b) exhibits how the normalized dissipation ϵ''_{zz}/α can be drastically manipulated through changes in μ. The type-I case at $\mu = \omega/2$ has an abrupt transition at $\beta = 0$. By increasing the tilt angle of the Weyl cones, the dissipative response broadens and ϵ''_{zz} is finite over a larger interval of chemical potentials. This can be of significance in anisotropic ENZ systems with dielectric losses where system parameters are tuned to control beam directivity [57] or EM wave absorption [58,59].
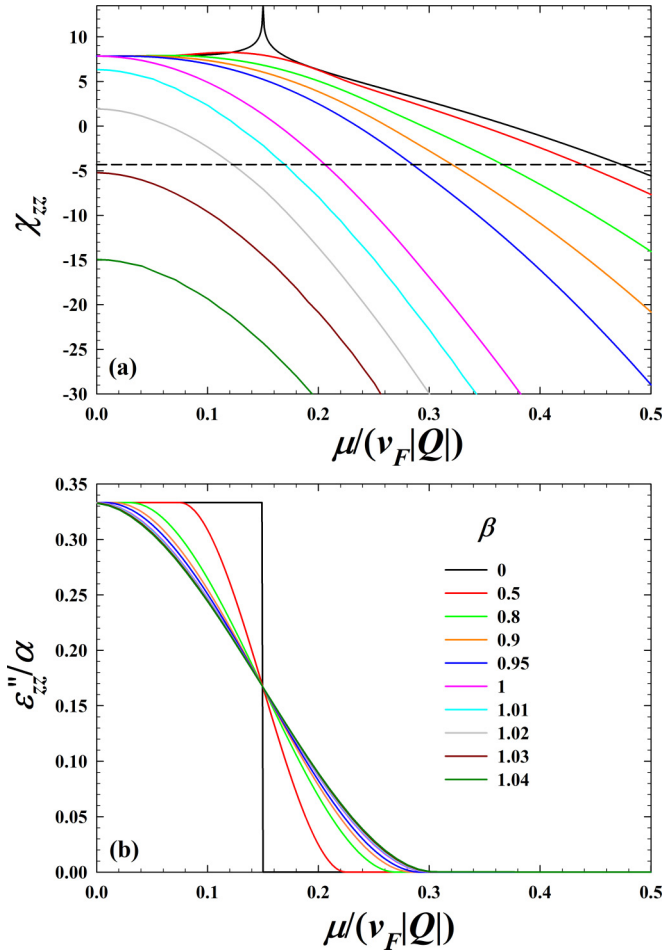
FIG. 2. (a) Illustration of how the susceptibility χ_{zz} is affected by changing the chemical potential in a Weyl semimetal. Increasing the tilt of the Weyl cones is seen to require a smaller μ for an ENZ response, corresponding to the intersection of the curves with the dashed line. (b) The normalized dissipative response ϵ''_{zz}/α. In both case, the normalized frequency corresponds to $\omega/(v_F|Q|) = 0.3$.

Next, in Fig. 3 we investigate how tilting of the Weyl cones influences the normalized susceptibility, Fig. 3(a), and dissipation, Fig. 3(b). Each curve represents a different μ, normalized as shown in the legend. Starting with $\mu = 0$ and $\beta < 1$, we observe that the permittivity is independent of the tilt, in agreement with Eq. (9). As β increases, however, χ_{zz} rapidly drops. The same type of behavior is seen in the other curves with small μ, where regions of relatively constant χ_{zz} diminish as μ increases. Thus, when the chemical potential is in the vicinity of the charge neutrality point, only a type-II WS, with $\beta > 1$, can exhibit ENZ behavior. As μ increases, each corresponding curve gets shifted down towards the ENZ line, so that smaller β can lead to a transition to a metallic-like state. Eventually, for the largest chemical potential shown, χ_{zz} cannot exhibit an ENZ response for any value of tilt. The observed peak at $\omega/\mu = 2$ (corresponding to $\mu/(v_F|Q|) = 0.15$) becomes diminished for other values of μ. For relatively weak chemical potentials, $\mu/(v_F|Q|) \leqslant 0.2$, an ENZ response is seen to be induced only when the WS is type-II. For $\beta \leqslant 1$, the ENZ regime arises only for larger μ. For example, the ENZ state is
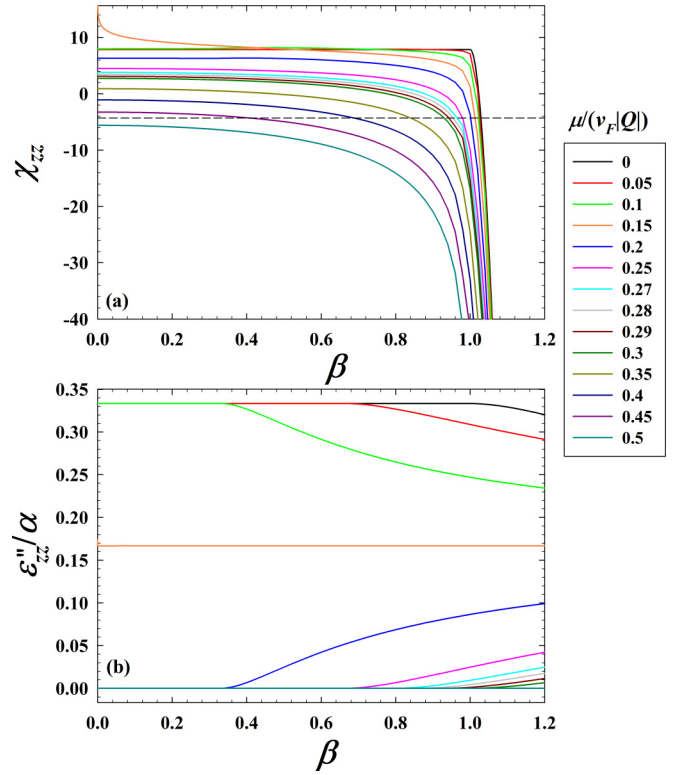

FIG. 3. Generation of an ENZ state through tilting of the Weyl cones: Through variation in β, panel (a) shows that χ_{zz} can transition to an ENZ state as represented by the dashed horizontal line. Panel (b) displays the imaginary component ϵ''_{zz}/α, where it is seen that β strongly affects the dissipation nature of the WS. The same μ values are used in both panels.

reached at $\beta \approx 0.4$, and $\mu/(v_F|Q|) = 0.45$. Thus, if the Weyl semimetal is to demonstrate an ENZ response, it should be type-I with sufficiently large μ, or it can be type-II with smaller μ. In either case, the dissipative component will be strongly affected, as Fig. 3(b) illustrates how cone tilt inclinations strongly influence ϵ''_{zz}. The normalized ϵ''_{zz} component is shown to not exceed 1/3. When $\mu/(v_F|Q|) = 0.15$ (or equivalently $\omega/\mu = 2$), the dimensionless ϵ''_{zz} is constant and has the value 1/6. Above this value of the chemical potential, the dissipative response tends to decline as β increases, while below it, the dissipation increases as β increases. At the charge neutrality point ϵ''_{zz}, it is unaffected by changes in the tilt for type-I, but for type-II ($\beta \gtrsim 1$), there is a weak decline, according to Eq. (10). Compared to Fig. 3(a), it is evident that for $\mu/(v_F|Q|) \gtrsim 0.3$, an ENZ response with zero effective loss can be achieved for a type-I WS. This situation could be relevant to waveguide structures, where localized electromagnetic waves propagate over long distances near the surface of the WS.

To estimate the feasibility of achieving an ENZ response in a type-II WS, we consider [23,60] $Q = 1 \, \text{nm}^{-1}$, $\mu = 0.08 \, \text{eV}$, $\beta = 1.02$, and $\omega = 0.2 \, \text{eV}$, to give $\epsilon'_{zz} \sim 0$, and $\epsilon''_{zz} \sim 0.5$. Although this estimate corresponds to a pair of points, to relate to a material such as TaAs, which has 12 pairs of Weyl cones, including 8 nodes with Fermi energy $\mu \approx 1 \, \text{meV}$ and 16 nodes with $\mu \approx 15 \, \text{meV}$, α should be multiplied by 4 and 8, respectively, to account for the additional nodes.
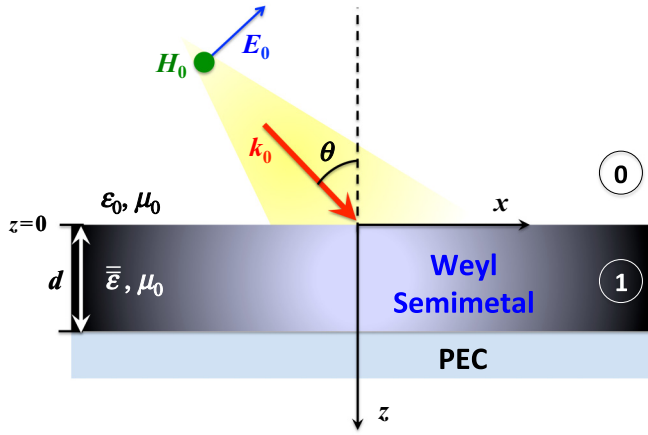
FIG. 4. Schematic of the configuration involving a Weyl semimetal in region ⓪ with width d atop a perfectly conducting substrate. The Weyl semimetal layer is exposed to an electromagnetic wave from the vacuum region ⓪. The incident electric field is polarized in the x-z plane, and the magnetic field is polarized along y. The incident wave vector $\boldsymbol{k}_0$ makes an angle θ with the z axis. The separation of the Weyl nodes is taken to be along the z axis.

III. PERFECT ABSORPTION IN WEYL SEMIMETAL STRUCTURES

In this section, we make use of the results for $\bar{\bar{\epsilon}}$ presented in the previous section to demonstrate how a WS structure in the ENZ regime can be tuned to exhibit perfect absorption of EM waves over a broad range of incident angles and system parameters, thus revealing a practical platform for the control of EM radiation.

A. Maxwell's equations and theory

We investigate the reflection and absorption of EM waves from the layered configuration shown in Fig. 4, which consists of a planar Weyl semimetal (region ①) adjacent to a metallic substrate with perfect conductivity (PEC). The electric field of the incident wave is polarized in the x-z plane, so that the permittivity component ϵ_{zz} plays a significant role in the overall EM response. The plane wave is incident from vacuum (region ⓪) with wave vector $\boldsymbol{k}_0$ also in the x-z plane: $\boldsymbol{k}_0 = \hat{\boldsymbol{x}}k_{0x} + \hat{\boldsymbol{z}}k_{0z}$. If the incident wave was propagating in the x-y plane, the TE and TM modes would become decoupled, and the reflectivity characteristics for the TM modes would not depend on the ϵ_{zz} component of the permittivity tensor. For propagation in the x-z plane, the TE and TM modes can no longer be separated, and the EM response of the WS structure is governed mainly by ϵ_{zz}.

The incident electric and magnetic fields thus have the following forms: $\boldsymbol{E} = (E_{x0}\hat{\boldsymbol{x}} + E_{z0}\hat{\boldsymbol{z}})e^{i(k_{0x}x + k_{0z}z - \omega t)}$, and $\boldsymbol{H} = H_{y0}\hat{\boldsymbol{y}}e^{i(k_{0x}x + k_{0z}z - \omega t)}$. Here k_{0x} is invariant across each layer, with $k_{0x} = k_0 \sin\theta$, $k_{0z} = k_0 \cos\theta$, and $k_0 = \omega/c$. For both regions ⓪ and ①, we implement Maxwell's equations for time harmonic fields,

$$\nabla \times \boldsymbol{E}_i = i\omega\mu_0 \boldsymbol{H}_i, \tag{15a}$$

$$\nabla \times \boldsymbol{H}_i = -i\omega \boldsymbol{D}_i, \tag{15b}$$

where $i = 0$ or 1. Within the WS, the propagation vector $\boldsymbol{k}_1$ replaces the spatial derivatives, transforming Maxwell's equations into the forms $\boldsymbol{k}_1 \times \boldsymbol{E}_1 = \omega\mu_0 \boldsymbol{H}_1$ and $\boldsymbol{k}_1 \times \boldsymbol{H}_1 = -\omega\bar{\bar{\epsilon}}\epsilon_0 \boldsymbol{E}_1$. These two equations together result in the following expression for the $\boldsymbol{E}_1$ field in $\boldsymbol{k}$ space:

$$\boldsymbol{k}_1 \times (\boldsymbol{k}_1 \times \boldsymbol{E}_1) = -k_0^2 \bar{\bar{\epsilon}} \boldsymbol{E}_1. \tag{16}$$

Using $\boldsymbol{k}_1 = k_{0x}\hat{\boldsymbol{x}} + k_{1z}\hat{\boldsymbol{z}}$ and the identity $\boldsymbol{k}_1 \times (\boldsymbol{k}_1 \times \boldsymbol{E}_1) = \boldsymbol{k}_1(\boldsymbol{k}_1 \boldsymbol{E}_1) - k_1^2 \boldsymbol{E}_1$ permits expansion of Eq. (16),

$$\begin{pmatrix} k_0^2\epsilon_{xx} - k_{1z}^2 & ik_0^2\gamma & k_{1z}k_{0x} \\ ik_0^2\gamma & k_\perp^2 - k_0^2\epsilon_{yy} & 0 \\ k_{0x}k_{1z} & 0 & k_0^2\epsilon_{zz} - k_{0x}^2 \end{pmatrix} \begin{pmatrix} E_{x1} \\ E_{y1} \\ E_{z1} \end{pmatrix} = 0, \tag{17}$$

where $k_\perp = \sqrt{k_{1z}^2 + k_{0x}^2}$, and $k_{1x} = k_{0x}$ due to translational invariance. The coupling of all three components of the $\boldsymbol{E}$ fields in Eq. (17) illustrates that although the electric field of the incident beam is polarized in the x-z plane, it can now acquire an additional y component when entering the gyrotropic medium. Similarly, despite having an initial polarization state along the x direction, the incident $\boldsymbol{H}$ field can also in general become polarized in all three directions once entering the WS. Thus, the EM wave exiting the WS structure can have a different overall polarization state that depends on the WS material and geometrical parameters.

B. Results and discussions

Since the incident beam propagates in the x-z plane with wave vector $\boldsymbol{k} = \hat{\boldsymbol{x}}k_{0x} + \hat{\boldsymbol{z}}k_{0z}$ (see Fig. 4), each component of $\bar{\bar{\epsilon}}$ must be accounted for in the EM response of the WS. Taking the determinant of the matrix in Eq. (17) and setting it equal to zero gives the dispersion equation for the WS that can be solved for k_{1z}:

$$\left(\epsilon_{xx}k_0^2 - k_\perp^2\right)\left(\epsilon_{xx}\epsilon_{zz}k_0^2 - \epsilon_{xx}k_{0x}^2 - \epsilon_{zz}k_{1z}^2\right)$$
$$+ k_0^2\left(k_{0x}^2 - \epsilon_{zz}k_0^2\right)\gamma^2 = 0. \tag{18}$$

Solving for the roots in Eq. (18) results in two types of solutions to k_{1z}, denoted by k_+ and k_-. We have

$$k_\pm^2 = \frac{k_0^2}{2\epsilon_{zz}}\Big[2\epsilon_{zz}\epsilon_\parallel - (\epsilon_\parallel + \epsilon_{zz})\sin^2\theta$$
$$\pm \sqrt{4\epsilon_{zz}^2\gamma^2 - 4\epsilon_{zz}\gamma^2\sin^2\theta + (\epsilon_\parallel - \epsilon_{zz})^2\sin^4\theta}\Big], \tag{19}$$

where $\epsilon_\parallel$ represents the components of $\bar{\bar{\epsilon}}$ parallel to the interfaces: $\epsilon_{xx} = \epsilon_{yy} = \epsilon_\parallel$. The dispersion equation (18) can now be compactly written in terms of the two types of waves:

$$k_0^2\epsilon_{zz}\left(k_{1z}^2 - k_+^2\right)\left(k_{1z}^2 - k_-^2\right) = 0. \tag{20}$$

For the configuration shown in Fig. 4, where the x-y plane is translationally invariant, the magnetic field components in the vacuum region, $\boldsymbol{H}_0$, are written in terms of incident and

reflected waves:

$$H_{x0} = r_3 e^{-ik_{0z}z} e^{ik_{0x}x}, \qquad (21a)$$

$$H_{y0} = (e^{ik_{0z}z} + r_1 e^{-ik_{0z}z}) e^{ik_{0x}x}, \qquad (21b)$$

$$H_{z0} = r_2 e^{-ik_{0z}z} e^{ik_{0x}x}, \qquad (21c)$$

where the x and z components represent the change of the incident polarization state upon reflecting from the Weyl semimetal. In other words, the coefficients r_2 and r_3 take into account the generation of additional polarization components upon interacting with the gyrotropic WS layer. Note that from the Maxwell's equation $\nabla \cdot \boldsymbol{H}_0 = 0$, there exists a simple relation between the coefficients r_2 and r_3:

$$r_3 = \frac{k_{0z}}{k_{0x}} r_2. \qquad (22)$$

From the magnetic field components above, we can use Eq. (15b) to easily deduce the electric field components for region ⓪.

For region ①, when using Maxwell's equations, we need to take into account the anisotropic nature of the WS. The general solution to the $\boldsymbol{E}$ field in the WS region is thus a linear combination of the four wave-vector components $k_{1z} = \{k_+, -k_+, k_-, -k_-\}$:

$$E_{y1} = (a_1 e^{ik_+z} + a_2 e^{-ik_+z} + a_3 e^{ik_-z} + a_4 e^{-ik_-z}) e^{ik_{0x}x}. \qquad (23)$$

To determine the coefficients $\{a_1, a_2, a_3, a_4\}$, it is necessary to invoke matching interface conditions and boundary conditions,

but first we must construct the remaining $\boldsymbol{E}$ and $\boldsymbol{H}$ fields. This is achieved via the two Maxwell's equations, Eqs. (15a) and (15b). First, using (15b) gives the following relations:

$$\frac{\partial H_{y1}}{\partial z} = i\omega\epsilon_0(\epsilon_\parallel E_{x1} + i\gamma E_{y1}), \qquad (24a)$$

$$\frac{\partial H_{x1}}{\partial z} - ik_{0x} H_{z1} = i\omega\epsilon_0(i\gamma E_{x1} - \epsilon_\parallel E_{y1}), \qquad (24b)$$

$$k_{0x} H_{y1} = -\omega\epsilon_0\epsilon_{zz} E_{z1}. \qquad (24c)$$

From Eq. (15a), we have

$$\frac{\partial E_{y1}}{\partial z} = -i\omega\mu_0 H_{x1}, \qquad (25a)$$

$$\frac{\partial E_{x1}}{\partial z} - ik_{0x} E_{z1} = i\omega\mu_0 H_{y1}, \qquad (25b)$$

$$k_{0x} E_{y1} = \omega\mu_0 H_{z1}, \qquad (25c)$$

where we have used the fact that x component is invariant, i.e., $\partial_x \rightarrow ik_{0x}$. Inserting Eq. (23) into the equations above, it is now possible to write all components of the EM field in terms of the coefficients $\{a_1, a_2, a_3, a_4\}$. For example, H_{x1} and H_{z1} are easily found from Eqs. (25a) and (25c) respectively. From that, one can solve Eq. (24b) for E_{x1}, and so on.

Upon matching the tangential electric and magnetic fields at the vacuum/WS interface, and using the boundary conditions of vanishing tangential electric fields at the ground plane, it is straightforward to determine the unknown coefficients. The first reflection coefficient r_1 is defined as $r_1 = 1 - r_0$, where

$$r_0 = \frac{2k_z^2[k_+q_-^2\cos(k_+d)\sin(k_-d) - [k_-q_+^2\cos(k_-d) + ik_{0z}(k_+^2 - k_-^2)\sin(k_-d)]\sin(k_+d)]}{k_-\cos(k_-d)[f_2\sin(k_+d) + i\epsilon_{zz}k_{0z}k_+(k_+^2 - k_-^2)\cos(k_+d)] + \sin(k_-d)[f_1k_+\cos(k_+d) - ik_{0z}k_z^2(k_+^2 - k_-^2)\sin(k_+d)]},$$

$$k_z = k_0\sqrt{\epsilon_{zz} - \sin^2\theta}, \quad q_\pm = \sqrt{\epsilon_\parallel k_0^2 - k_{0x}^2 - k_\pm^2}, \quad f_1 = k_z^2 q_-^2 - \epsilon_{zz}k_{0z}^2 q_+^2, \quad f_2 = -k_z^2 q_+^2 + \epsilon_{zz}k_{0z}^2 q_-^2. \qquad (26)$$

The r_2 coefficient is expressed compactly in terms of r_1 and r_0:

$$r_2 = \frac{k_{0x}\gamma\left[k_z^2(r_1 + 1)\sin(k_-d) - i\epsilon_{zz}k_{0z}k_-r_0\cos(k_-d)\right]}{\epsilon_{zz}q_+^2[ik_{0z}\sin(k_-d) - k_-\cos(k_-d)]}. \qquad (27)$$

In the absence of gyrotropy, $\gamma = 0$, $r_2 = r_3 = 0$, and the corresponding reflection coefficient r_1 reduces to

$$r_1 = 1 - \frac{2k_-}{k_- + ik_{0z}\epsilon_\parallel\cot(k_-d)}, \qquad (28)$$

in which $k_- = \sqrt{\epsilon_\parallel(k_0^2 - k_{0x}^2/\epsilon_{zz})}$. Thus, when $\gamma = 0$, the reflection coefficient reverts to that of a diagonally anisotropic medium [59], as it should. When the gyrotropic parameter vanishes, the incident electric field that is polarized in the x-z plane, remains in that plane after interacting with the WS.

In determining the absorptance A of the WS system, it is beneficial to study the energy flow in the vacuum region. To this end, we consider the time-averaged Poynting vector in the

direction perpendicular to the interfaces (the z direction), $S_{z0} = \Re\{E_{x0}H_{y0}^* - E_{y0}H_{x0}^*\}/2$. Inserting the electric and magnetic fields calculated for region ⓪ above, we find

$$A = 1 - |r_1|^2 - |r_2|^2 - |r_3|^2. \qquad (29)$$

Here A is defined as S_{z0}/S_0, where $S_0 \equiv k_{0z}/(2\epsilon_0\omega)$ is the time-averaged Poynting vector for a plane wave traveling in the z direction.

Having established the methods for determining the absorption and reflection coefficients, we now consider a range of material and geometrical parameters that lead to perfect absorption in the ENZ regime where $\epsilon'_{zz} \approx 0$. The dissipative component ϵ''_{zz}, on the other hand, can vary, as it plays a crucial role in how electromagnetic energy is absorbed by the system. For a given WS width d, frequency ω of the incident wave, and orientation θ, the absorptance [Eq. (29)] can be calculated by incorporating the results of Sec. II, which gives the various μ and β that lead to an ENZ response and allows the remaining components of the tensor $\bar{\bar{\epsilon}}$ to be determined via Eqs. (5b)–(5d).
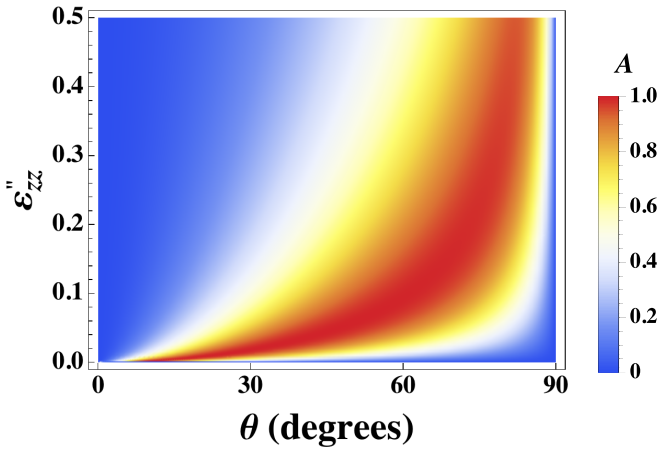
FIG. 5. Color map demonstrating how the absorptance A varies as a function of the incident angle θ and dissipation ϵ_{zz}''. The system is in the ENZ regime, whereby $\epsilon_{zz}' = 0$. The normalized frequency is set to $\omega/(v_F|Q|) = 0.3$, and $d/\lambda = 1/100$.

FIG. 6. The absorptance A as a function of normalized chemical potential $\mu/(v_F|Q|)$ for a type-II WS structure having an ENZ response. Three different orientations θ of the incident beam are shown. The tilting parameter corresponds to $\beta = 1.01$, the normalized frequency is $\omega/(v_F|Q|) = 0.3$, and $d/\lambda = 1/100$.

The results from Sec. II offer clear guides for identifying ENZ regions of the parameter space. For example, it was observed in Fig. 1 that for the range of frequencies considered, it is necessary for the chemical potential to be nonzero for the dissipative component ϵ_{zz}'' to have significant variations. We show below that ϵ_{zz}'' plays a crucial role in determining how much of the incident beam is perfectly absorbed [58] and that strong absorption can arise over a broader range of θ when ϵ_{zz}'' corresponds to moderate loss and also when it is very small. Thus, we focus on the more interesting cases when μ is away from the charge neutrality point ($\mu = 0$). Indeed, Figs. 1(c)–1(f) showed that by having a finite μ, ϵ_{zz}'' can be continuously tuned from zero to a situation having appreciable dissipation. If the dissipation vanishes entirely, the type of perfect absorption studied here does not arise since all incoming waves are reflected back from the ground plane. Increasing the loss makes it possible at appropriate frequencies and orientations of the incident beam, for the waves in the WS to destructively interact and ultimately dissipate through Joule heating. For most of the frequencies of interest here, which satisfy $\omega/(v_F|Q|) < 2\mu/(v_F|Q|)$, the component of the permittivity parallel to the interfaces $\epsilon_\parallel$ [Eq. (5b)], is purely real, as it has no interband contribution to the optical conductivity.

To illustrate how ϵ_{zz}'' directly impacts the absorption characteristics of the WS structure shown in Fig. 4, we present in Fig. 5 a color map that depicts the absorptance A as a function of the incident angle θ and the loss ϵ_{zz}''. We consider the scenario where the WS is assumed to have an ENZ response, $\epsilon_{zz}' = 0$, so that ϵ_{zz} is described entirely by its imaginary component. As was extensively discussed in Sec. II, ϵ_{zz}'' generally depends on several system parameters. Here, however, in order to isolate the effects of dissipation and its relation to angles of high absorption, ϵ_{zz}'' varies independently. In this example, we have $\mu/(v_F|Q|) = 0.2$ and $\gamma = 3$. As Fig. 5 shows, depending on ϵ_{zz}'', perfect absorption can be achieved for virtually any incident angle. Thus, for example, to determine the WS parameters needed to achieve perfect absorption around normal incidence ($\theta \sim 0°$), it is only necessary to identify
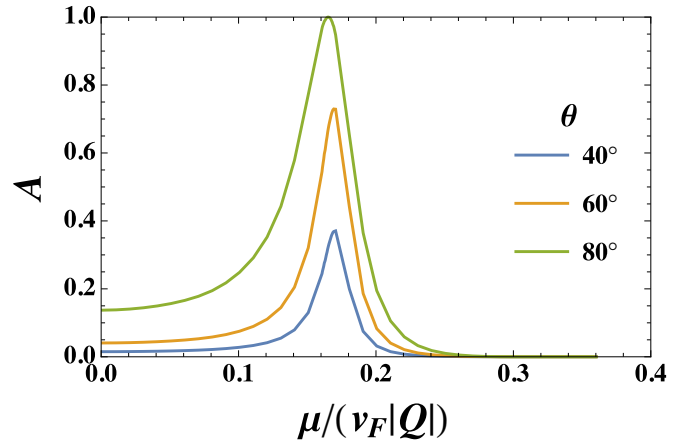
configurations where $\epsilon_{zz}' \approx 0$ for small ϵ_{zz}''. The fact that for angles near normal incidence, the loss must be extremely weak for perfect absorption is consistent with the response of isotropic ENZ slabs [1]. On the other hand, to have the entire incident wave's energy absorbed at broader angles ($\theta \sim 90°$), the ENZ structure must exhibit greater dissipation, with $\epsilon_{zz}'' \gtrsim 0.3$. The occurrence of perfect absorption in thin, anisotropic ENZ layers is one of the hallmarks of coherent perfect absorption [58], which couples light to a fast wave propagating along the WS interface. A main feature of coherent perfect absorption is the intricate dependence on the real and imaginary parts of ϵ_{zz}, which can lead to the formation of localized waves inside very narrow regions. The perfect conductive substrate serves as the reflecting surface that results in the destructive interference of incoming waves, so that under the proper conditions, the incident beam becomes completely absorbed.

Previously, in Fig. 2, we found that by tuning the chemical potential, not only can an ENZ response be achieved but also the loss in the WS can be highly sensitive to changes in μ. To study the effects that variations in μ have on the EM response of the WS, in Fig. 6, we present the absorptance of the WS structure as a function of the normalized μ. Three different orientations of the incident wave are considered, as shown in the legend. We consider a representative value for a type-II case, $\beta = 1.01$, which according to Fig. 2 puts the system in the ENZ regime at $\mu/(v_F|Q|) \approx 0.17$. For this value of the chemical potential, the loss corresponds to $\epsilon_{zz}'' \approx 0.3$. The remaining components of the permittivity tensor are calculated from Eqs. (5b) and (5d), resulting in $\epsilon_\parallel \approx 2.8$ and $\gamma \approx 2.9$. Note that while conventional absorbers are often restricted by their relatively large thicknesses, remarkably the WS layer exhibited here has an extremely subwavelength thickness, corresponding to $d/\lambda = 1/100$. Thus, for an incident wavelength of $\lambda \sim 10 \, \mu m$; this implies $d \sim 100 \, nm$. We note that the results are relatively insensitive to $\epsilon_\parallel$. Moreover, for the narrow WS widths considered here, the off-diagonal gyrotropic component γ has a limited effect on the results, so that Eq. (28)
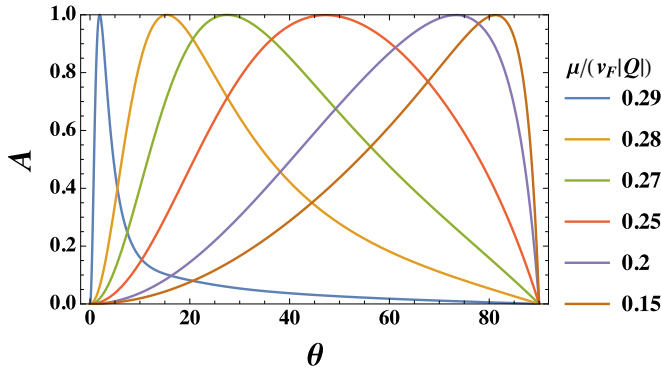
FIG. 7. The absorptance A as a function of incident angle θ. Several normalized chemical potentials are considered (see legend). For $\mu/(v_F|Q|) = 0.29, 0.28, 0.27, 0.25$, and 0.2, the Weyl semimetal should be type-I, with $\beta \sim 0.94, 0.96, 0.97, 0.98$, and 0.99, respectively. To achieve perfect absorptance for larger incident angles that more closely approach grazing ($\theta \rightarrow 90°$), the $\mu/(v_F|Q|) = 0.15$ case requires a type-II WS, with $\beta \sim 1.01$. In all cases, the normalized frequency is set to $\omega/(v_F|Q|) = 0.3$ and $d/\lambda = 1/100$.

is often suitable for describing the reflection characteristics over a broad range of parameters. Overall, we find that the phenomena presented here are dictated mainly by ϵ_{zz}. This is consistent with the results of Fig. 6, where weak absorption occurs for smaller θ, but when $\theta = 80°$, there is complete absorption. As Fig. 5 showed, increases in the dissipative component ϵ_{zz}'' require that the incident waves approach the interface at larger θ in order to be absorbed perfectly.

We now proceed to show that for certain μ and tilting β, both type-I and type-II WS systems can completely absorb the incident EM radiation over a relatively wide range of incident wave orientations θ. In Fig. 7, the absorptance is shown as a function of θ for a few normalized μ (see legend). For chemical potentials outside of this range, the imaginary component ϵ_{zz}'' is either too small or too large to achieve perfect absorption (see Fig. 2). The subwavelength slab width is again fixed at $d/\lambda = 1/100$, and the incident wave has a frequency corresponding to $\omega/(v_F|Q|) = 0.3$. Beginning with the largest chemical potential, $\mu/(v_F|Q|) = 0.29$, we find that perfect absorption occurs at close to normal incidence. This is because as Fig. 2(b) showed, when $\mu/(v_F|Q|) = 0.29$,

a very small amount of loss is present. Therefore, from Fig. 5, θ must be small in order for the incident beam to couple to the EM modes responsible for perfect absorption. Besides having loss, it is also necessary for $\epsilon_{zz}' \approx 0$, which as in Fig. 2(a) shows, only small $\beta < 1$ in this case results in an ENZ response. By decreasing the chemical potential, the WS becomes more dissipative. Thus we find that each of the perfect absorption peaks in Fig. 7 gets shifted toward grazing incidence ($\theta \rightarrow 90°$). This, however, requires greater tilting of the Weyl cones to achieve $\epsilon_{zz}' = 0$, which in some instances corresponds to a type-II situation where β exceeds unity (see Fig. 2).

Finally, to show the importance of using subwavelength WS structures in the ENZ regime to achieve perfect absorption, we investigate how changes in the width d of the WS (see Fig. 4) affects the absorption properties of the system. In Fig. 8, the color maps depict the absorptance as a function of the normalized width d/λ and incident angle θ. Both WS types are considered: (a) type-II with $\beta = 1.01$ and (b) type-I with $\beta = 0.96$. In Fig. 8(a), $\mu/(v_F|Q|) = 0.15$, which corresponds to $\epsilon_{zz} \approx 0.12 + 0.37i$, and a gyrotropic parameter of $\gamma \approx 3$. In Fig. 8(b), the chemical potential is increased to $\mu/(v_F|Q|) = 0.28$, so that the WS still has ϵ_{zz} in the ENZ regime, but with very little loss, corresponding to a small imaginary component $\epsilon_{zz}'' \approx 0.005$. The gyrotropic parameter is relatively unchanged from the previous case, with now $\gamma \approx 3.1$. For both panels, the normalized frequency is set at $\omega/(v_F|Q|) = 0.3$. It is evident that the type-II WS in Fig. 8(a) admits perfect absorption over larger angles, and that the normalized width should satisfy $d/\lambda \lesssim 1/10$ for appreciable absorption. As the incident beam is directed more toward grazing angles ($\theta \rightarrow 90°$), it is apparent that d must be continuously reduced in order for the system to remain a perfect absorber. For widths that are larger than the range shown here, coupling between the incident beam and the WS system becomes substantially diminished as additional reflections are introduced that destroy the previous coherent effects. For the type-I case [Fig. 8(b)], the widths again need to be subwavelength, satisfying $d/\lambda \lesssim 1/10$, and as mentioned above, perfect absorption arises at small inclinations of the incident beam due to the weakly dissipative nature of ϵ_{zz} for these system parameters. We also see a trend similar to the type-II case in Fig. 8(a), where increases in θ require thinner WS widths to achieve $A \approx 1$.
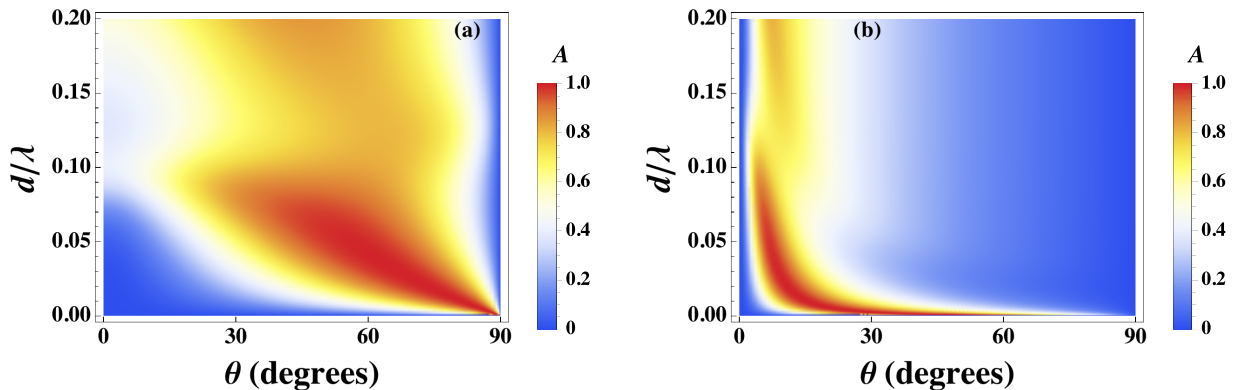

FIG. 8. Color maps illustrating the perfect absorption regions for various normalized widths d/λ and incident angles θ. In panel (a), $\beta \sim 1.01$ and $\mu/(v_F|Q|) = 0.15$. In panel (b), $\beta \sim 0.96$ and $\mu/(v_F|Q|) = 0.28$. In both panels, the normalized frequency is set to $\omega/(v_F|Q|) = 0.3$,

IV. CONCLUSIONS

In this paper, we studied the dielectric response of anisotropic type-I and type-II tilted Weyl semimetals. We presented both analytic and numerical results that characterized each component of the permittivity tensor. We showed that depending on the Weyl cone tilt, chemical potential, and electromagnetic wave frequency, the component of the permittivity tensor normal to the interfaces can achieve an ϵ-near-zero (ENZ) response. At the charge neutrality point, we showed that only type-II Weyl semimetals can exhibit an ENZ response. We also discussed how losses near the ENZ frequency can be controlled and effectively eliminated by properly adjusting the Weyl cone tilt and chemical potential. Making use of the calculated permittivity tensor for the Weyl semimetal, we also investigated the electromagnetic response of a Weyl semimetal structure consisting of a planar Weyl semimetal adjacent to a perfect conductor in vacuum. Our findings showed that thin Weyl semimetals with an ENZ response can be employed as coherent perfect absorbers for nearly any incident angle by choosing the proper geometrical and material parameters.

[1] M. Silveirinha and N. Engheta, Phys. Rev. Lett. **97**, 157403 (2006).

[2] A. Alù, M. G. Silveirinha, A. Salandrino, and N. Engheta, Phys. Rev. B **75**, 155410 (2007).

[3] H. Galinski, G. Favraud, H. Dong, J. S. T. Gongora, G. Favaro, M. Döbeli, R. Spolenak, A. Fratalocchi, and F. Capasso, Light: Sci. Appl. **6**, e16233 (2017).

[4] B. Edwards, A. Alù, M. E. Young, M. Silveirinha, and N. Engheta, Phys. Rev. Lett. **100**, 033903 (2008).

[5] R. Liu, Q. Cheng, T. Hand, J. J. Mock, T. J. Cui, S. A. Cummer, and D. R. Smith, Phys. Rev. Lett. **100**, 023903 (2008).

[6] V. N. Smolyaninova, B. Yost, K. Zander, M. S. Osofsky, H. Kim, S. Saha, R. L. Greene, and I. I. Smolyaninov, Sci. Rep. **4**, 7321 (2014).

[7] D. C. Adams, S. Inampudi, T. Ribaudo, D. Slocum, S. Vangala, N. A. Kuhta, W. D. Goodhue, V. A. Podolskiy, and D. Wasserman, Phys. Rev. Lett. **107**, 133901 (2011).

[8] M. Mattheakis, C. A. Valagiannopoulos, and E. Kaxiras, Phys. Rev. B **94**, 201404(R) (2016).

[9] Z. Wang, Y. Sun, X.-Q. Chen, C. Franchini, G. Xu, H. Weng, X. Dai, and Z. Fang, Phys. Rev. B **85**, 195320 (2012).

[10] A. A. Burkov and L. Balents, Phys. Rev. Lett. **107**, 127205 (2011).

[11] S.-M. Huang, S.-Y. Xu, I. Belopolski, C.-C. Lee, G. Chang, B. Wang, N. Alidoust, G. Bian, M. Neupane, C. Zhang, S. Jia, A. Bansil, H. Lin, and M. Z. Hasan, Nat. Commun. **6**, 7373 (2015).

[12] B. Q. Lv, H. M. Weng, B. B. Fu, X. P. Wang, H. Miao, J. Ma, P. Richard, X. C. Huang, L. X. Zhao, G. F. Chen, Z. Fang, X. Dai, T. Qian, and H. Ding, Phys. Rev. X **5**, 031013 (2015).

[13] H. Wely, I. Z. Phys. **56**, 330 (1929).

[14] M. Z. Hasan and C. L. Kane, Rev. Mod. Phys. **82**, 3045 (2010).

[15] X.-L. Qi and S.-C. Zhang, Rev. Mod. Phys. **83**, 1057 (2011).

[16] A. A. Zyuzin and A. A. Burkov, Phys. Rev. B **86**, 115133 (2012).

[17] I. Belopolski, S. Y. Xu, D. S. Sanchez, G. Chang, C. Guo, M. Neupane, H. Zheng, C. C. Lee, S. M. Huang, G. Bian, N. Alidoust, T. R. Chang, B. K. Wang, X. Zhang, A. Bansil, H. T. Jeng, H. Lin, S. Jia, and M. Z. Hasan, Phys. Rev. Lett. **116**, 066802 (2016).

[18] X. Wan, A. M. Turner, A. Vishwanath, and S. Y. Savrasov, Phys. Rev. B **83**, 205101 (2011).

[19] G. Xu, H. Weng, Z. Wang, X. Dai, and Z. Fang, Phys. Rev. Lett. **107**, 186806 (2011).

[20] S.-Y. Xu, N. Alidoust, I. Belopolski, Z. Yuan, G. Bian, T.-R. Chang, H. Zheng, V. N. Strocov, D. S. Sanchez, G. Chang, C. Zhang, D. Mou, Y. Wu, L. Huang, C.-C. Lee, S.-M. Huang, B. Wang, A. Bansil, H.-T. Jeng, T. Neupert, A. Kaminski, H. Lin, S. Jia, and M. Zahid Hasan, Nat. Phys. **11**, 748 (2015).

[21] H. Weng, C. Fang, Z. Fang, B. A. Bernevig, and X. Dai, Phys. Rev. X **5**, 011029 (2015).

[22] C. Shekhar, A. K. Nayak, Y. Sun, M. Schmidt, M. Nicklas, I. Leermakers, U. Zeitler, Y. Skourski, J. Wosnitza, Z. Liu, Y. Chen, W. Schnelle, H. Borrmann, Y. Grin, C. Felser, and B. Yan, Nat. Phys. **11**, 645 (2015).

[23] S.-Y. Xu, I. Belopolski, N. Alidoust, M. Neupane, G. Bian, C. Zhang, R. Sankar, G. Chang, Z. Yuan, C.-C. Lee, S.-M. Huang, H. Zheng, J. Ma, D. S. Sanchez, B. Wang, A. Bansil, F. Chou, P. P. Shibayev, H. Lin, S. Jia, and M. Z. Hasan, Science **349**, 613 (2015).

[24] B. Xu, Y. M. Dai, L. X. Zhao, K. Wang, R. Yang, W. Zhang, J. Y. Liu, H. Xiao, G. F. Chen, A. J. Taylor, D. A. Yarotski, R. P. Prasankumar, and X. G. Qiu, Phys. Rev. B **93**, 121110 (2016).

[25] S. Chi, Z. Li, Y. Xie, Y. Zhao, Z. Wang, L. Li, H. Yu, G. Wang, H. Weng, H. Zhang, and J. Wang, arXiv:1705.05086.

[26] A. A. Soluyanov, D. Gresch, Z. Wang, Q. Wu, M. Troyer, X. Dai, and B. A. Bernevig, Nature (London) **527**, 495 (2015).

[27] Y. Sun, S.-C. Wu, M. N. Ali, C. Felser, and B. Yan, Phys. Rev. B **92**, 161107 (2015).

[28] A. Liang, J. Huang, S. Nie, Y. Ding, Q. Gao, C. Hu, S. He, Y. Zhang, C. Wang, B. Shen, J. Liu, P. Ai, L. Yu, X. Sun, W. Zhao, S. Lv, D. Liu, C. Li, Y. Zhang, Y. Hu, Y. Xu, L. Zhao, G. Liu, Z. Mao, X. Jia, F. Zhang, S. Zhang, F. Yang, Z. Wang, Q. Peng, H. Weng, X. Dai, Z. Fang, Z. Xu, C. Chen, and X. J. Zhou, arXiv:1604.01706.

[29] S.-Y. Xu, N. Alidoust, G. Chang, H. Lu, B. Singh, I. Belopolski, D. Sanchez, X. Zhang, G. Bian, H. Zheng, M.-A. Husanu, Y. Bian, S.-M. Huang, C.-H. Hsu, T.-R. Chang, H.-T. Jeng, A. Bansil, V. N. Strocov, H. Lin, S. Jia, and M. Z. Hasan, arXiv:1603.07318.

[30] G. Autès, D. Gresch, M. Troyer, A. A. Soluyanov, and O. V. Yazyev, Phys. Rev. Lett. **117**, 066402 (2016).

[31] I. Belopolski, S.-Y. Xu, Y. Ishida, X. Pan, P. Yu, D. S. Sanchez, M. Neupane, N. Alidoust, G. Chang, T.-R. Chang, Y. Wu, G. Bian, H. Zheng, S.-M. Huang, C.-C. Lee, D. Mou, L. Huang, Y.

Song, B. Wang, G. Wang, Y.-W. Yeh, N. Yao, J. Rault, P. Lefevre, F. Bertran, H.-T. Jeng, T. Kondo, A. Kaminski, H. Lin, Z. Liu, F. Song, S. Shin, and M. Z. Hasan, arXiv:1512.09099.

[32] Y. Wu, N. Hyun Jo, D. Mou, L. Huang, S. L. Bud'ko, P. C. Canfield, and A. Kaminski, Phys Rev B **94**, 121113 (2016).

[33] P. Huhtala and G. E. Volovik, JETP **94**, 853 (2002).

[34] G. E. Volovik and M. A. Zubkov, Nucl. Phys. B **881**, 514 (2014).

[35] F. Detassis, L. Fritz, and S. Grubinskas, Phys. Rev. B **96**, 195157 (2017).

[36] S. P. Mukherjee and J. P. Carbotte, Phys. Rev. B **96**, 085114 (2017).

[37] S. P. Mukherjee and J. P. Carbotte, Phys. Rev. B **97**, 035144 (2018).

[38] M. A. Kats, D. Sharma, J. Lin, P. Genevet, R. Blanchard, Z. Yang, M. M. Qazilbash, D. N. Basov, S. Ramanathan, and F. Capasso, Appl. Phys. Lett. **101**, 221101 (2012).

[39] J. Zhao, Q. Cheng, J. Chen, M. Q. Qi, W. X. Jiang, and T. J. Cui, New J. Phys. **15**, 043049 (2013).

[40] D. Shrekenhamer, W.-C. Chen, and W. J. Padilla, Phys. Rev. Lett. **110**, 177403 (2013).

[41] Y. Yao, R. Shankar, M. A. Kats, Y. Song, J. Kong, M. Loncar, and F. Capasso, Nano Lett. **14**, 6526 (2014).

[42] A. A. Zyuzin and V. A. Zyuzin, Phys. Rev. B **92**, 115310 (2015).

[43] M. Chinotti, A. Pal, W. J. Ren, C. Petrovic, and L. Degiorgi, Phys. Rev. B **94**, 245101 (2016)

[44] E. Haubold, K. Koepernik, D. Efremov, S. Khim, A. Fedorov, Y. Kushnirenko, J. van den Brink, S. Wurmehl, B. Buchner, T. K. Kim, M. Hoesch, K. Sumida, K. Taguchi, T. Yoshikawa, A. Kimura, T. Okuda, and S. V. Borisenko, Phys. Rev. B **95**, 241108 (2017).

[45] T. Timusk, J. P. Carbotte, C. C. Homes, D. N. Basov, and S. G. Sharapov, Phys. Rev. B **87**, 235121 (2013).

[46] Q. Li, D. E. Kharzeev, C. Zhang, Y. Huang, I. Pletikosic, A. V. Fedorov, R. D. Zhong, J. A. Schneeloch, G. D. Gu, and T. Valla, Nat. Phys. **12**, 550 (2016).

[47] R. Y. Chen, S. J. Zhang, J. A. Schneeloch, C. Zhang, Q. Li, G. D. Gu, and N. L. Wang, Phys. Rev. B **92**, 075107 (2015).

[48] C.-X. Liu, P. Ye, and X.-L. Qi, Phys. Rev. B **87**, 235306 (2013).

[49] J. Zhou, H.-R. Chang, and D. Xiao, Phys. Rev. B **91**, 035114 (2015).

[50] D. E. Kharzeev, R. D. Pisarski, and H.-U. Yee, Phys. Rev. Lett. **115**, 236402 (2015).

[51] A. B. Sushkov, J. B. Hofmann, G. S. Jenkins, J. Ishikawa, S. Nakatsuji, S. Das Sarma, and H. D. Drew, Phys. Rev. B **92**, 241108 (2015).

[52] J. Hofmann and S. Das Sarma, Phys. Rev. B **91**, 241108 (2015).

[53] O. V. Kotov and Yu. E. Lozovik, Phys. Rev. B **93**, 235417 (2016).

[54] M. Kargarian, M. Randeria, and N. Trivedi, Sci. Rep. **5**, 12683 (2015).

[55] D. J. Bergman and Y. M. Strelniker, Phys. Rev. Lett. **80**, 857 (1998).

[56] R. W. Bomantara and J. Gong, Phys. Rev. B **94**, 235447 (2016).

[57] K. Halterman, S. Feng, and V. C. Nguyen, Phys. Rev. B **84**, 075162 (2011).

[58] S. Feng and K. Halterman, Phys. Rev. B **86**, 165103 (2012).

[59] K. Halterman and J. M. Elson, Opt. Express **22**, 7337 (2014).

[60] Q. Ma, S.-Y. Xu, C.-K. Chan, C.-L. Zhang, G. Chang, Y. Lin, W. Xie, T. Palacios, H. Lin, S. Jia, P. A. Lee, P. Jarillo-Herrero, and N. Gedik, Nat. Phys. **13**, 842 (2017).